Article

Mapping Sub-Metre 3D Land-Sea Coral Reefscapes Using Superspectral WorldView-3 Satellite Stereoimagery

Antoine Collin [1,2,*], **Mark Andel** [3], **David Lecchini** [2,4] **and Joachim Claudet** [2,5]

1. Coastal GeoEcological Lab, Ecole Pratique des Hautes Etudes (EPHE), PSL University, 35800 Dinard, France
2. Laboratoire d'Excellence "CORAIL", 66100 Perpignan, France; david.lecchini@ephe.psl.eu (D.L.); joachim.claudet@cnrs.fr (J.C.)
3. Digitalglobe Foundation, Westminster, CO 80234, USA; mark.andel@digitalglobe.com
4. CRIOBE, EPHE-UPVD-CNRS, PSL University, 98729 Moorea, French Polynesia
5. Maison des Océans, CRIOBE, EPHE-UPVD-CNRS, PSL University, 75005 Paris, France
* Correspondence: antoine.collin@ephe.psl.eu

Abstract: Shallow coral reefs ensure a wide portfolio of ecosystem services, from fish provisioning to tourism, that support more than 500 million people worldwide. The protection and sustainable management of these pivotal ecosystems require fine-scale but large-extent mapping of their 3D composition. The sub-metre spaceborne imagery can neatly produce such an expected product using multispectral stereo-imagery. We built the first 3D land-sea coral reefscape mapping using the 0.3 m superspectral WorldView-3 stereo-imagery. An array of 13 land use/land cover and sea use/sea cover habitats were classified using sea-, ground- and air-truth data. The satellite-derived topography and bathymetry reached vertical accuracies of 1.11 and 0.89 m, respectively. The value added of the eight mid-infrared (MIR) channels specific to the WorldView-3 was quantified using the classification overall accuracy (OA). With no topobathymetry, the best combination included the eight-band optical (visible + near-infrared) and the MIR8, which boosted the basic blue-green-red OA by 9.58%. The classes that most benefited from this MIR information were the land use "roof" and land cover "soil" classes. The addition of the satellite-derived topobathymetry to the optical+MIR1 produced the best full combination, increasing the basic OA by 9.73%, and reinforcing the "roof" and "soil" distinction.

Keywords: satellite; superspectral; VHR; topobathymetry; LULC; SUSC; Moorea Island

1. Introduction

Tropical shallow hard coral reef ecosystems provide numerous and valuable services to local socio-economies, such as fish and seafood provisioning, coastal protection, or wealthy recreational activities [1]. These services have been estimated to support more than 500 million people worldwide [2]. Even though coral reefs cover only 0.1% of the oceans, they host 25% of all marine identified species [3]. However, anthropocenic changes, embodied by both sea level, sea temperature and sea acidification rises and also sedimentation related to watershed deforestation and land claiming, are strongly threatening these pivotal ecosystems [4].

The protection and sustainable management of these ecosystems requires us to adopt an integrated view of the seamless land- and seascape at a high spatial resolution, adequate to meet local stakeholders' expectations [5]. Even if the global, thus coarse (>1 m pixel size), products are insightful for assessing coral reef trends, the very high spatial (i.e., <1 m pixel size) mapping of the land use land cover (LULC) and the sea use sea cover (SUSC) constitutes a fitting response to needs of local users, managers and decision-makers. Either passive or active, airborne imagery can successfully provide some spectro-spatial combinations able to generate coastal topography and bathymetry using unmanned airborne vehicles [6,7], and map sub-metre LULC and SUSC using hyper-/multi-spectral camera [8] or multi-spectral light detection and ranging (LiDAR) system [9]. However, the

manned or unmanned airborne limitations, tied to the elevation-specific flight planning and the relatively small surveyed area, impede their utilization for regional mapping [10]. The sub-metre spaceborne imagery has emerged as a tool of interest given its capability to capture large extents with a very high spatial resolution, despite its purchase cost [11]. Around 2000, IKONOS (1999) and QuickBird-2 (2001) became the first satellite sensors collecting imagery at 1 m pixel size across regional scales. These civilian and commercial pioneers were followed by sub-metre United States WorldView-1, -2, -3, -4 (2007, 2009, 2014, 2016), GeoEye-1 (2008), SkySat series (2013–2017), French Pleiades-1A and -1B (2011 and 2012), Korean Kompsat-3 and -3A (2012 and 2015), United Kingdom TripleSat (2015), and Chinese Gaofen-2 (2014), Jilin-1 (2015), Superview-1 (2018) [12]. In addition to their spatial resolution capability inherent to the panchromatic band, most of these sensors acquire four spectral bands: the visible (VIS) blue, green, red (BGR), and the optical near-infrared (NIR). Three outliers thereupon appear: the panchromatic WorldView-1, the optical 8-band WorldView-2, and the optical+mid-infrared (MIR) 16-band WorldView-3. The WorldView-2 improved the bathymetry mapping [5], the coral cover and health mapping [13,14], and the seamless LULC/SUSC mapping [11]. The WorldView-3 augmented the bathymetry [15], mineral [16], hydrocarbon [17], lithological [18], salt marsh [19], tropical forest [20], coral reef [8], and even urban plastic [21] mapping.

Furthermore, the spaceborne sub-metre LULC mapping was significantly enhanced by the (tri-)stereo-acquisition of the same scene, offering the opportunity to produce seamless land-sea digital surface models (DSMs), using the photogrammetry for land and the ratio transform for sea [22]. Horizontal and vertical accuracies of the land DSM-derived stereo-Pleiades-1 have been quantified at 0.53 and 0.65 m, respectively [12]. The addition of the topographic band to the spectral information has been shown to significantly improve spaceborne sub-metre LULC mapping [12]. Even if the novelty of the latter work relied on the sole use of a spaceborne stereo-imagery, the bathymetry and the SUSC mapping were not examined. An integration of the terrestrial and marine DSM into the spaceborne sub-metre spectral dataset was elsewhere useful in mapping the seamless coral reefscape in Japan using Google Earth imagery [23], but it was not derived from a sole spaceborne by-product. To our knowledge, a unique study has focused on the land-sea coral reefscape mapping using a sole spaceborne sub-metre stereo-imagery [24].

Despite the use of the WorldView-3 stereo-imagery to produce land-sea DSM, the authors had not previously investigated the added value of the 16-band superspectral dataset to map LULC and SUSC, simultaneously. In this paper, we innovatively propose to classify sub-metre LULC and SUSC of a coral reefscape using a sole spaceborne stereo-imagery, from which the topographic, bathymetric and superspectral information are derived. The scene studied was acquired over the complex coral reefscape of Moorea Island (French Polynesia, South Pacific) using a WorldView-3 stereo-imagery (Figure 1). The chosen area exhibits representative eight LULC and five SUSC classes, and encompasses steep volcanic vegetated watersheds, flat rural coastal areas, and a reef-dominated lagoon. An set of five issues will be considered: (1) the added value of the Coastal and yellow bands to the basic BGR classification accuracy; (2) the added value of the Red Edge (RE), NIR1 and NIR2 bands to the basic BGR classification accuracy; (3) the added value of the MIR bands to the basic BGR classification accuracy; (4) the influence of the topobathymetry (i.e., land-sea DSM) on the basic, visible, optical and optical+MIR datasets' classification performance; and (5) all four previous questions considered at the class-level.
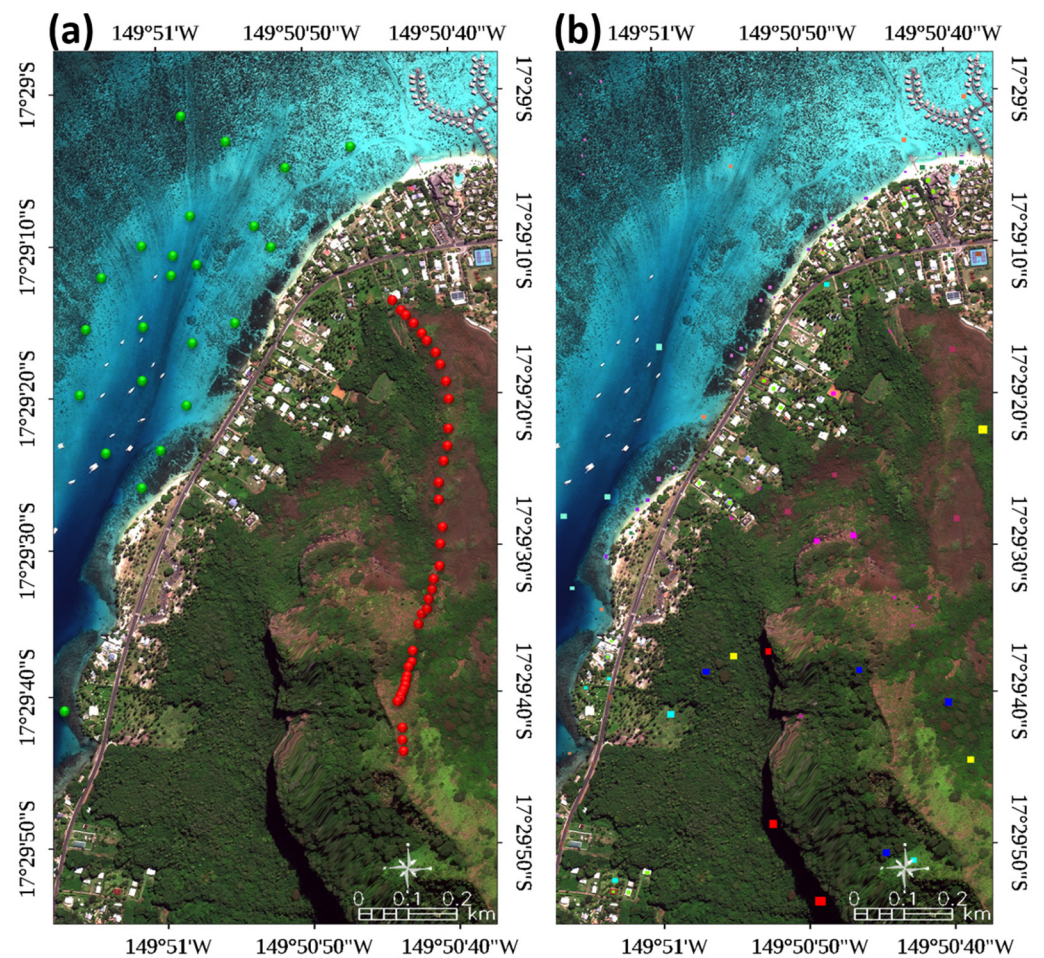
Figure 1. Natural-coloured WorldView-3 imagery (0.3 m × 0.3 m, 3017 × 5937 pixels) of the study area on Moorea Island (French Polynesia). (**a**) The red and green spheres represent 32 topographic and 35 bathymetric calibration/validation datasets; (**b**) the array of 105 multi-colour rectangles represents 78,000 pixels of 13 habitats, each one composed by 3000 calibration and 3000 validation pixels.

2. Materials and Methods

2.1. Study Site

The study site is located on the north shore of Moorea Island (17°32′ S, 149°50′ W) in French Polynesia (Figure 1). Moorea is a 1.6 million-year-old volcanic island which at its highest point reaches 1207 m and extends over 187 km^2, divided into 134 km^2 and 53 km^2 of land and sea areas, respectively. While being in the vicinity of Tahiti, the capital of French Polynesia, Moorea, is considered as a life-size laboratory, given its large array of land-sea spatial patterns and multi-scale socio-ecological processes [25]. The spatial features include rain and dry forests, volcanic and laterite soils, coconut and banana crops, urban infrastructures, coralligeneous sand, reef pavement, fringing and barrier reefs. The territory is changing rapidly due to the doubling of the local population in 40 years [26], the conversion of forest to pineapple crops and the urban growth. The lagoon hosts traditional fishing activities and is experiencing an increase in tourism activities. The test area, extending over 1.61 km^2, is composed of a complex land-sea coral reefscape, selected to embrace all the previously mentioned components.

2.2. Land-, Sea- and Air-Truth Data

The topobathymetry extraction requires XYZ control points for both land and sea realms [24]. The topographic DSM was calibrated and validated by 20 and 12 ground

control points (see red spheres in Figure 1a), surveyed in September 2018 with a Mobile Mapper 120 provided with a 20 Hz Differential-GPS+GLONASS position output, ensuring a maintained 0.3 m accuracy. The sampling distribution was not optimal because it was constrained by the need to use a single pathway that ran along a crest surrounded by steep ravines. The bathymetric DSM was calibrated and validated by 20 and 15 sea control points, retrieved from the digitized French Navy chart (identified as 6657, based on a 1966-to-1972 hydrographic campaign originally referenced to the lowest astronomical tide, see green spheres in Figure 1a). Despite the gap in timing between the waterborne soundings and the spaceborne acquisition, the absence of major local events in the seascape enabled the freely available hydrographic soundings to be used, for the sake of transferability. Both topographic and bathymetric control points were then horizontally referenced to the UTM 6 South projection into the WGS-84 datum, and vertically zeroed to the mean sea level.

A suite of 13 habitats (Figure 1b) were inspected using geolocated handborne photoquadrats for land classes and geolocated airborne for sea classes. Photoquadrats were taken with an Olympus Tough TG-4 provided with BGR bands (16 million pixels each), while aerial pictures were monitored using a DJI Mavic Pro Platinum collecting BGR bands (12 million pixels) at 35 m altitude (height above the mean sea level). A series of 90 photoquadrats and 90 aerial photographs were orthorectified [8] to distinguish 10 classes, representative of an average land-sea coral reefscape (Table 1). Five land and five sea classes were each constituted of 30 and 30 seed pixels neighbourly and evenly grown to 3000 calibration and 3000 validation pixels, respectively. The three remaining classes, namely forest, roof and shadow, were straightforwardly characterized by 3000 calibration and 3000 validation pixels visually selected on the satellite imagery.

Table 1. Description of the 13 land use/land cover and sea use/sea cover classes.

Class Name	Class Description	Class Colour
Forest	Wet arborescent stratum	
Wood	Wet arbustive stratum	
Grass	Wet herbaceous stratum	
Dry vegetation	Wind and sun exposed forest, wood or grass	
Soil	Bare volcanic or lateritic substratum	
Roof	Wooden or metallic house covering	
Road	Tarmac way	
Shadow	Tree or house shading	
Backshore	Emerged coral sand	
Foreshore	Shallow coral sand	
Nearshore	Mid coral sand	
Offshore	Deep coral sand	
Coral reefs	Scleractinian and coralline algae	

2.3. Spaceborne Dataset

Launched on 13 August 2014, the commercial WorldView-3 spearheads the choice of sub-metre civilian satellite, given its hyperspatial and superspectral capabilities, namely one panchromatic band at 0.3 m, five VIS + three NIR bands at 1.2 m, and eight MIR bands at 3.7 m. The pansharpening technique can successfully produce 16 spectral bands at 0.3 m spatial resolution ([27], Figure 2).
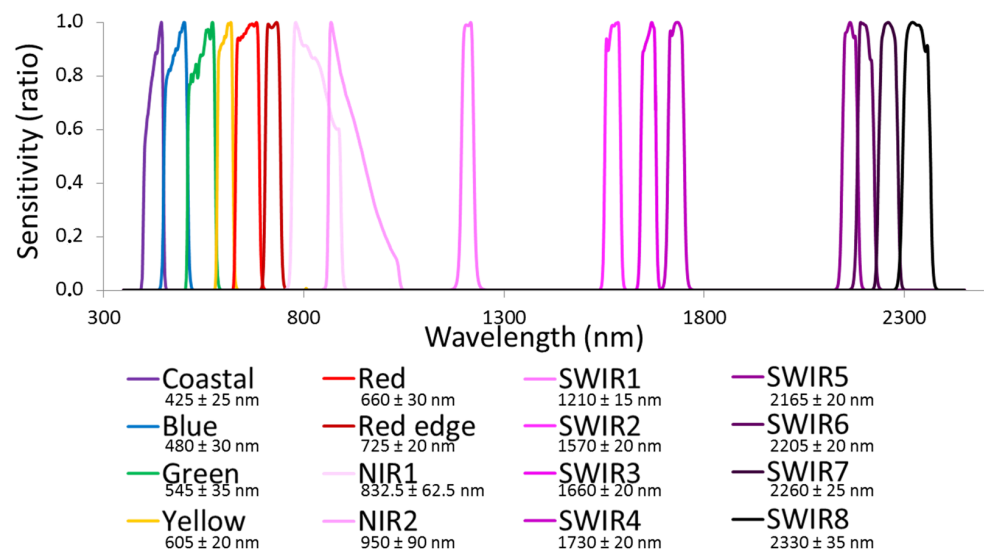
Figure 2. Lineplot of the superspectral (16 bands) WorldView-3 sensor's sensitivity as a function of their wavelengths.

Provided with a daily revisit, this sensor leverages a swath width of 13.1 km and length of 112 km. The WorldView-3 dataset used here is a stereo-imagery acquired on 18 July 2018 at 20:35:38 UTC (Figure 3a, Table 2) and 20:36:39 UTC, respectively (Figure 3b, Table 2).
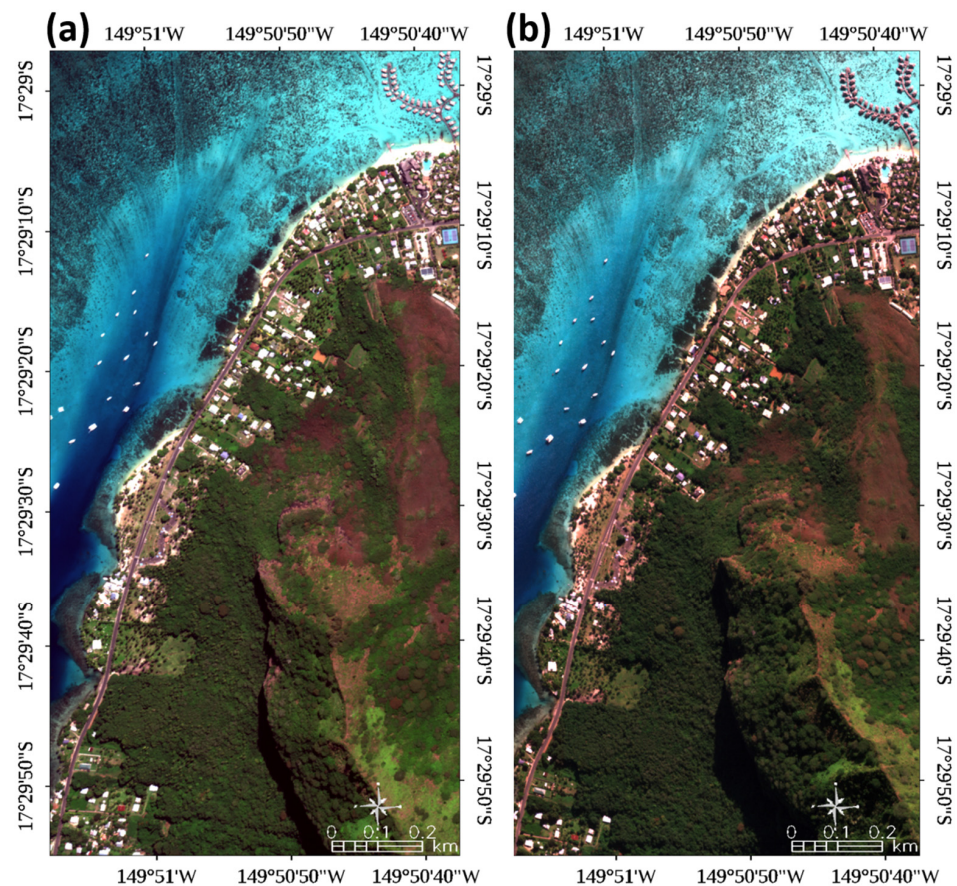
Figure 3. Natural-coloured WorldView-3 imageries of the study area, taken on 18 July 2018, over the north shore of Moorea Island (French Polynesia). (**a**) Imagery #1 taken with 26.4° off-nadir viewing angle; (**b**) Imagery #2 taken with 16.5° off-nadir viewing angle.

Table 2. WorldView-3 specifications related to the stereo-imagery acquisition over the study site.

Parameters	Imagery #1	Imagery #2
Date	12 July 2018	12 July 2018
Time (UTC)	20:35:38	20:36:39
Mean viewing angle		
In-track (in °)	23.6	−12.6
Cross-track (in °)	12.2	10.8
Off-nadir (in °)	26.4	16.5
Satellite azimuth (in °)	34.3	148.6
Satellite elevation (in °)	60.7	71.9
Sun azimuth (in °)	29.9	29.7
Sun elevation (in °)	45.0	45.1

2.4. Spaceborne Topographic DSM

The building of the satellite-based topographic DSM requires both panchromatic imageries to be radiometrically converted from digital number to top-of-atmosphere radiance, then to bottom-of-atmosphere reflectance values by considering the calibration factors (.IMD file), the atmosphere composition and sun irradiance (see [5] for details). The reflectance imageries were used to retrieve a 3D point cloud using a dense point matching algorithm [28]. The matching algorithm seeks for the pairwise pixels of two imageries by shortening the epipolar 2D to 1D, based on the rational polynomial coefficients (RPCs), then by reducing the length of the epipolar line with the global multi-resolution terrain elevation data 2010 dataset. The point cloud was then gridded at 0.3 m by converting the XY coordinates into the WGS84 datum, UTM zone 6S, and referencing in Z to the mean sea level (Figure 4). The topographic validation accuracy was estimated by the mean absolute error (MAE) and the root mean square error (RMSE) between the modeled and observed values ($N = 12$). The MAE and RMSE attained 0.84 and 1.11 m, which corroborates the results from previous WorldView-3 works [24].

2.5. Spaceborne Bathymetric DSM

The creation of the satellite-based bathymetric DSM relies on the use of a single multispectral imagery that needs to be both radiometrically and geometrically corrected, as well as pansharpened. The imagery #2 was selected for this purpose since it displayed the lowest off-nadir viewing angle (Table 2). Following the radiometric correction (see Section 2.4), the VIS+NIR multispectral reflectance imagery was orthorectified using the RPCs and the 20 ground control points, as well as the corresponding panchromatic reflectance imagery. Among seven sharpening methods, the Gram-Schmidt pansharpening procedure yielded the best visual results, and it was then implemented so as to produce a VIS+NIR dataset at 0.3 m pixel size (see [5] for details). The resulting sub-metre eight-band dataset was subjected to the radiative transfer model, called the ratio transform [29]. This standard bathymetric model makes use of the fact that light absorption by water varies with wavebands. It can thereafter determine the bathymetry (z), as follows:

$$z = a_1 \left(\frac{ln[R_w(\lambda_i) - R_\infty(\lambda_i)]}{ln[R_w(\lambda_j) - R_\infty(\lambda_j)]} \right) - a_0 \tag{1}$$

where a_0 is the intercept to match the mean sea level, a_1 is the slope converting the relative to absolute bathymetry (20 calibration sea control points), R_w is the reflectance related to the waveband λ_i, and R_∞ is the reflectance over deep water. The MAE and RMSE bathymetric validation ($N = 15$) accuracy reached 0.74 and 0.89 m, echoing the findings from previous WorldView-3 studies [15,24].
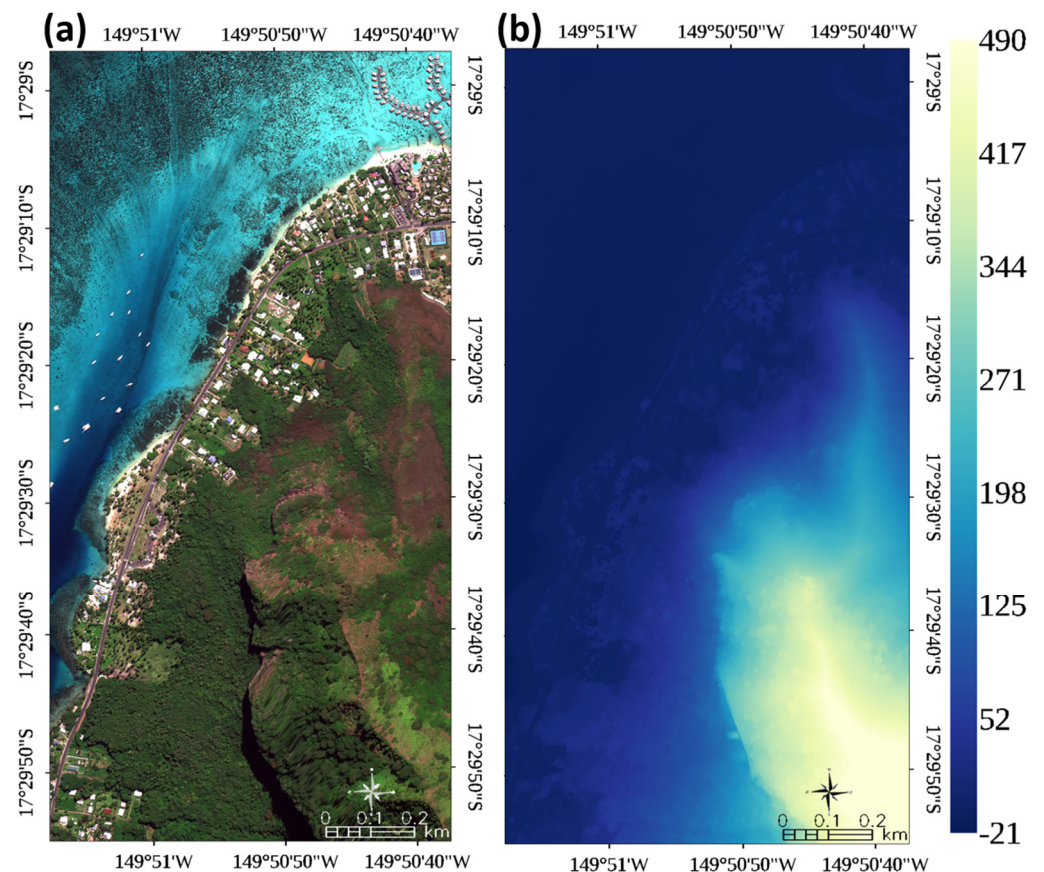
Figure 4. (**a**) Natural-coloured orthorectified WorldView-3 imagery of the study area; (**b**) topo-bathymetric digital surface model (in m) derived from the combination of a photogrammetry-based stereo-panchromatic imagery for land and a ratio transform model for sea, both derived from the same WorldView-3 stereo-imagery. The colour scale on the right indicates the estimated height and depth below sea-level of different parts of the image.

2.6. Habitat Classification

The habitat mapping stemmed from the superspectral capabilities of the WorldView-3 sensor. In addition to the pansharpened optical (VIS+NIR) reflectance, the eight-band MIR contribution to landscape (and not seascape given its water absorption) mapping was tested, which necessitated radiometric and geometric corrections purposed to the pansharpening enhancement (see [19] for WorldView-3 pansharpening). An output of 16 spectral bands at 0.3 m was used as input predictors for a supervised classification based on the commonly used probabilistic maximum likelihood (ML) algorithm. This learner assumes that the statistics for each class in each spectral band are normally distributed, enabling the probability that a given pixel belongs to a specific class to be estimated.

The 3000 calibration pixels per class were used to build the ML model, while the 3000 validation pixels per class were intended for computing the confusion matrix (CM), from which the omission, commission misclassification (or error) and overall accuracy (OA) were drawn. These accuracy metrics were based only on the multi-colour rectangular regions of interest (see Figure 1b), and not on the whole scene. The omission misclassification corresponded to the rate at which sites were erroneously omitted from the correct class in the classified map, while the commission misclassification embodied the rate at which sites were correctly classified as ground-truth sites but were erroneously omitted from the correct class in the classified map. The OA and CM were used to analyze gain patterns at the scene and the class scale, respectively. First, the VIS, NIR and MIR spectral contributions were assessed by, respectively, adding the Coastal and yellow, RE-NIR1-NIR2, and MIR1-MIR2-MIR3-MIR4-MIR5-MIR6-MIR7-MIR8 bands, to the basic BGR combination.

Second, the spatial contribution of the land-sea DSM was evaluated for the three spectral blendings. Third, the best predictions were further analyzed at the class level.

3. Results

Firstly, the contributions of the WorldView-3 spectral VIS, NIR and MIR were quantified for the LULC-SUSC classification accuracy. Secondly, the WorldView-3 spatial topobathymetric DSM was evaluated. Thirdly, the highest spectral and topobathymetric effects were assessed at the class scale.

3.1. WorldView-3 Superspectral Land-Sea Habitat Mapping

The classification performance of the BGR basic dataset provided a satisfactory OA of 89.15% (Figure 5a). On the one hand, the addition of the coastal and yellow predictors, yielding the VIS combination, increased the basic OA by 2.69% (Figure 5b). On the other hand, the addition of the RE, NIR1 and NIR2 to the VIS combination, so as to produce the optical dataset, augmented the basic OA by 8.79% (Figure 5c).
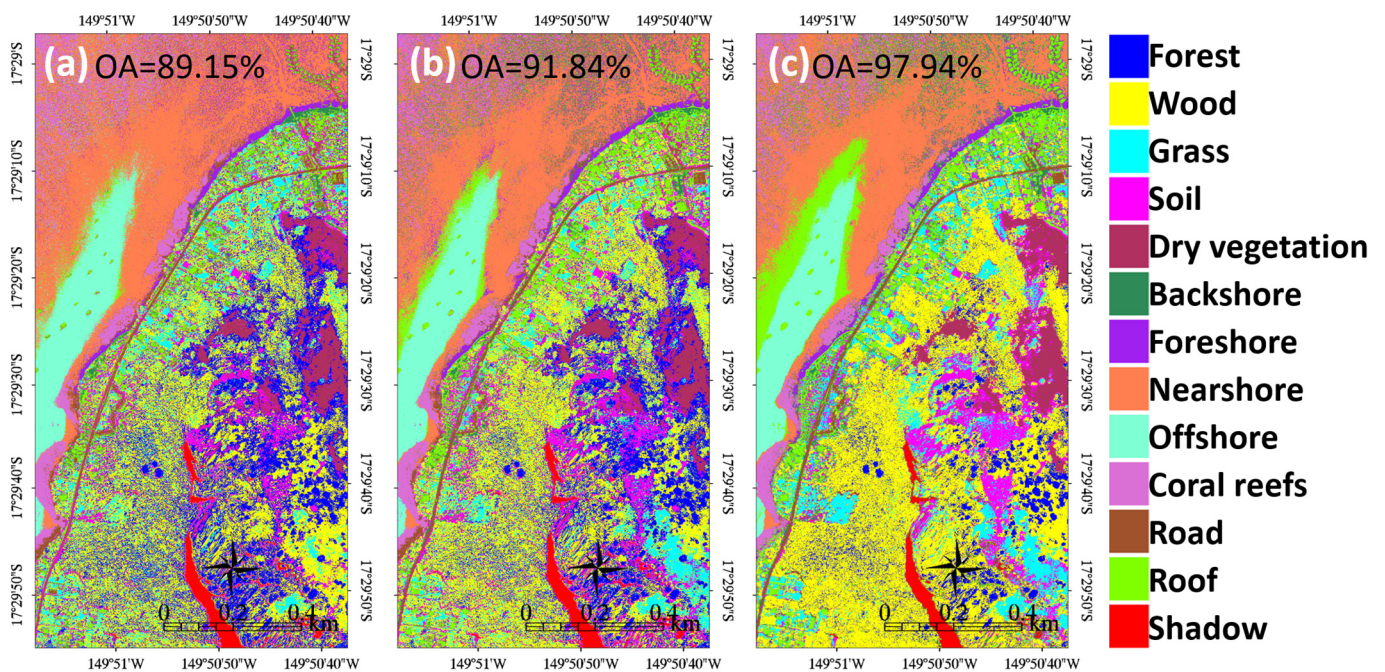
Figure 5. Maximum likelihood classification maps of the land-sea coral reefscape using WorldView-3: (**a**) basic dataset (blue-green-red); (**b**) visible dataset (Coastal-blue-green-yellow-red); (**c**) optical dataset (Coastal-blue-green-yellow-red-Red Edge-Near-InfraRed1-Near-InfraRed2).

The addition of the eight MIR spectral bands, individually, to the optical dataset showed a high mean contribution of 9.52% (Figure 6). However, some subtle patterns could be highlighted: the MIR8, MIR7, MIR2, MIR5 contributed to a gain of the basic OA (9.58%, 9.57%, 9.53% and 9.51%, respectively); the MIR3, MIR4 and MIR6 contributed to the mean increase of 9.5%; and the MIR1 contributed to an enhancement of 9.47%. Given that the optical boosting to the basic OA was 8.79%, all MIR bands brought novel information to discriminate LULC-SUSC.
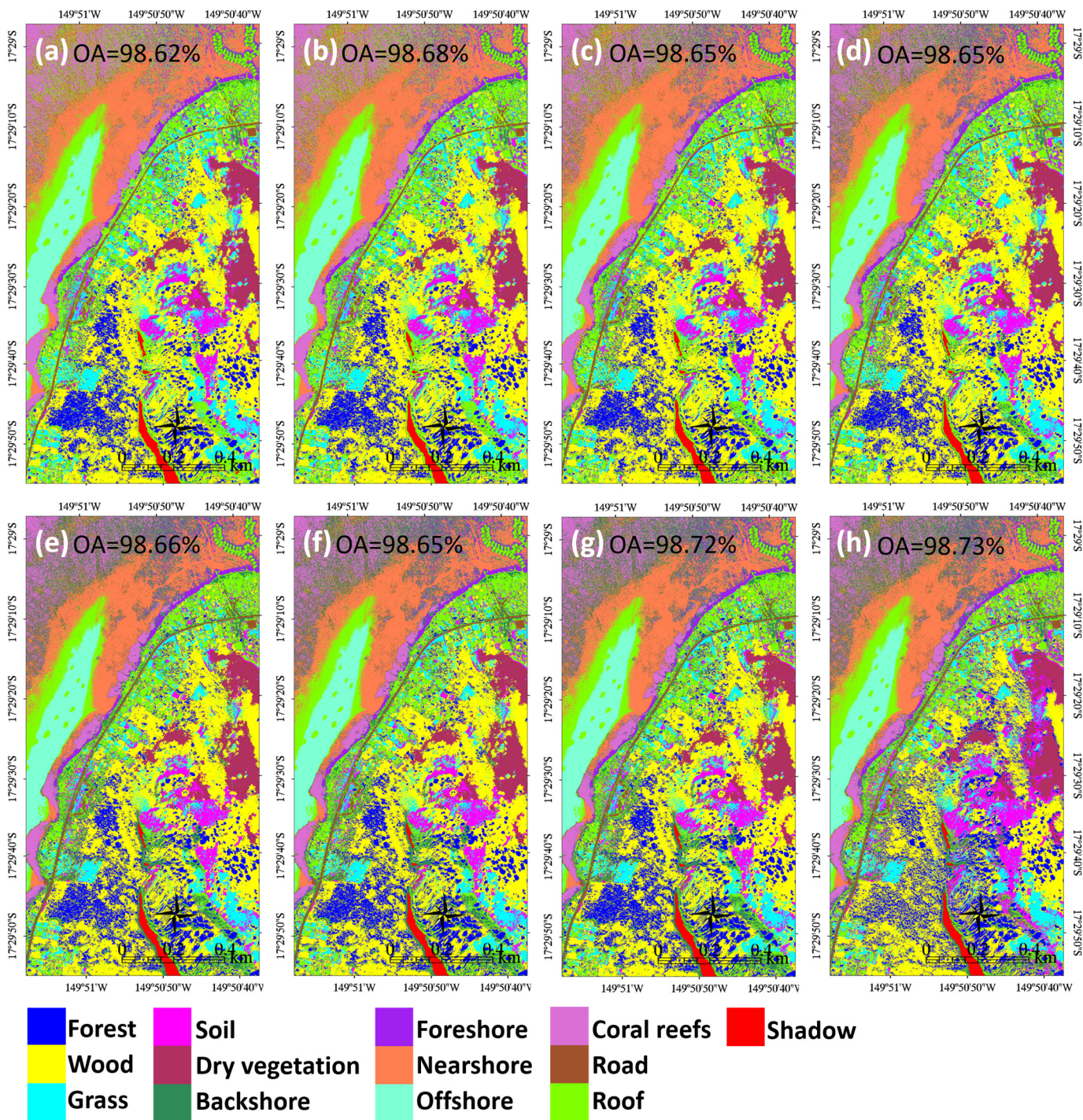
Figure 6. Maximum likelihood classification maps of the land-sea coral reefscape using WorldView-3 optical dataset with: (**a**) Mid-InfraRed1 (MIR1); (**b**) MIR2; (**c**) MIR3; (**d**) MIR4; (**e**) MIR5; (**f**) MIR6; (**g**) MIR7; (**h**) MIR8.

3.2. WorldView-3 Topobathymetry into Land-Sea Habitat Mapping

The evaluation of the influence of the WorldView-3-derived topobathymetry followed the same procedure as in 3.1. The addition of the DSM to the BGR basic dataset increased the OA by 2.74% (Figure 7a). The addition of the DSM to the VIS combination augmented the basic OA by 5.44% (Figure 7b). The addition of the DSM to the optical dataset enhanced the basic OA by 9.15% (Figure 7c).

Figure 7. Maximum likelihood classification maps of the land-sea coral reefscape using WorldView-3 topobathymetric digital surface model with: (**a**) basic dataset (blue-green-red); (**b**) visible dataset (Coastal-blue-green-yellow-red); (**c**) optical dataset (Coastal-blue-green-yellow-red-Red Edge-Near-InfraRed1-Near-InfraRed2).

The addition of the DSM to the eight MIR spectral bands (individually added to the optical dataset) showed a high mean contribution of 9.55% (Figure 8), slightly better than the MIR bands with no DSM (Figure 6). Some variations still appeared: the MIR1, MIR8, and MIR7 contributed to the best gains of the basic OA (9.73%, 9.69%, and 9.60%, respectively); the MIR5 and MIR6 contributed to the mean boost of 9.53% and 9.51%; and the MIR4, MIR2 and MIR3 contributed to the least increases of 9.47%, 9.45% and 9.42%. Since the DSM-added optical contribution to the basic OA was 9.15%, all MIR bands continued to provide insights for improving LULC-SUSC mapping.

3.3. WorldView-3 Land-Sea Habitat Mapping at the Class Scale

The best OA for the WorldView-3 multispectral and superspectral, deprived of and provided with the inner topobathymetry, were further studied at the class level by comparing their confusion matrices with that for the basic BGR (Figure 9).

Concerning the multispectral level, the optical dataset strongly improved the discrimination of the grass (27.7%) and wood (19.27%), as well as the road (15.93%). The coral reefs also benefited from a better differentiation (1.2%), partly due to the decline in omission misclassification with the offshore (−0.93%). The addition of the topobathymetric DSM confirmed the greater distinction between previous classes (grass, 27.5%; wood, 26.27%; and road, 19.27%), but also improved the ability to detect the roof (23.87%) and soil (8.53%) classes. The coral reefs' separability was also heightened (1.87%) owing to the decrease in omission misclassification with the nearshore (−0.57%).

Regarding the superspectral degree, the optical dataset enhanced with the MIR8 empowered to distinguish grass (27.6%), wood (25.53%), roof (22.87%), road (20.03%), and soil (14.6%) classes. The coral reefs were also better discerned (2.07%) given the reduction in omission misclassification with the nearshore (−0.93%). The integration of the DSM information to the optical+MIR1 dataset still upgraded the classification of the grass (27.33%), wood (27.1%), roof (24.5%), road (20.67%), and soil (12.97%). Nevertheless, the coral reefs' classification remained rigorously constant (2.07%).
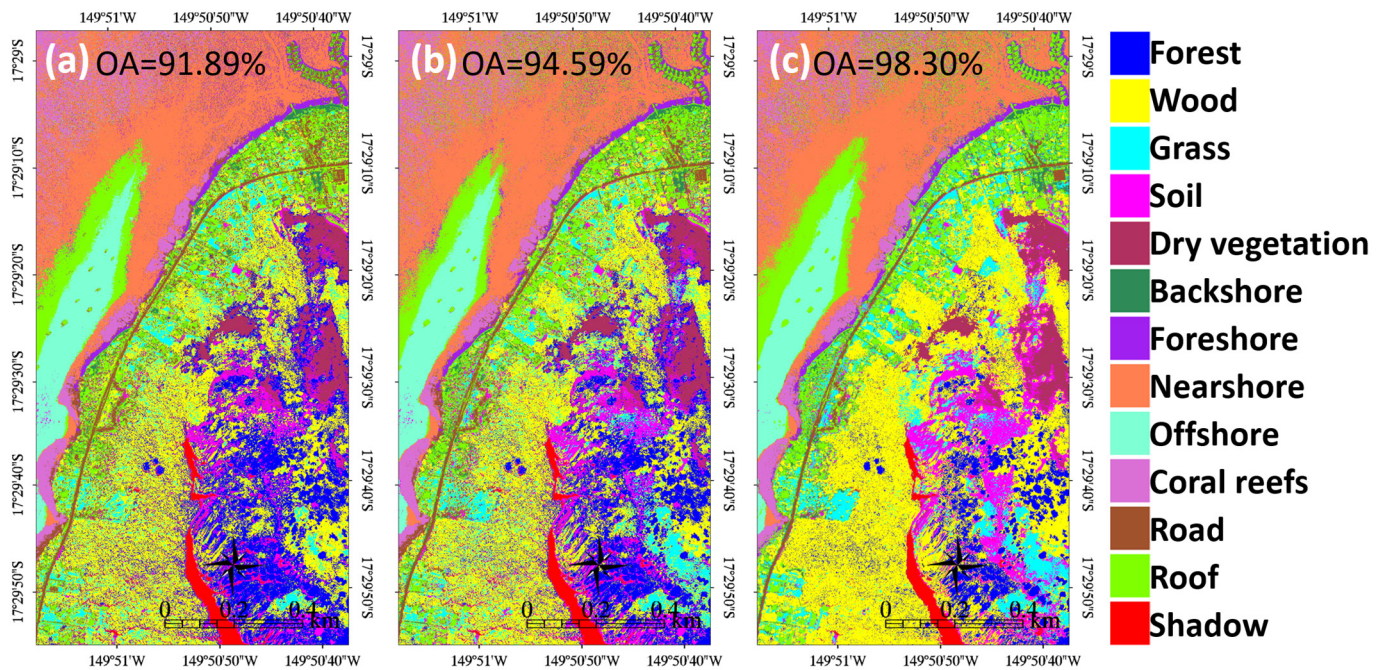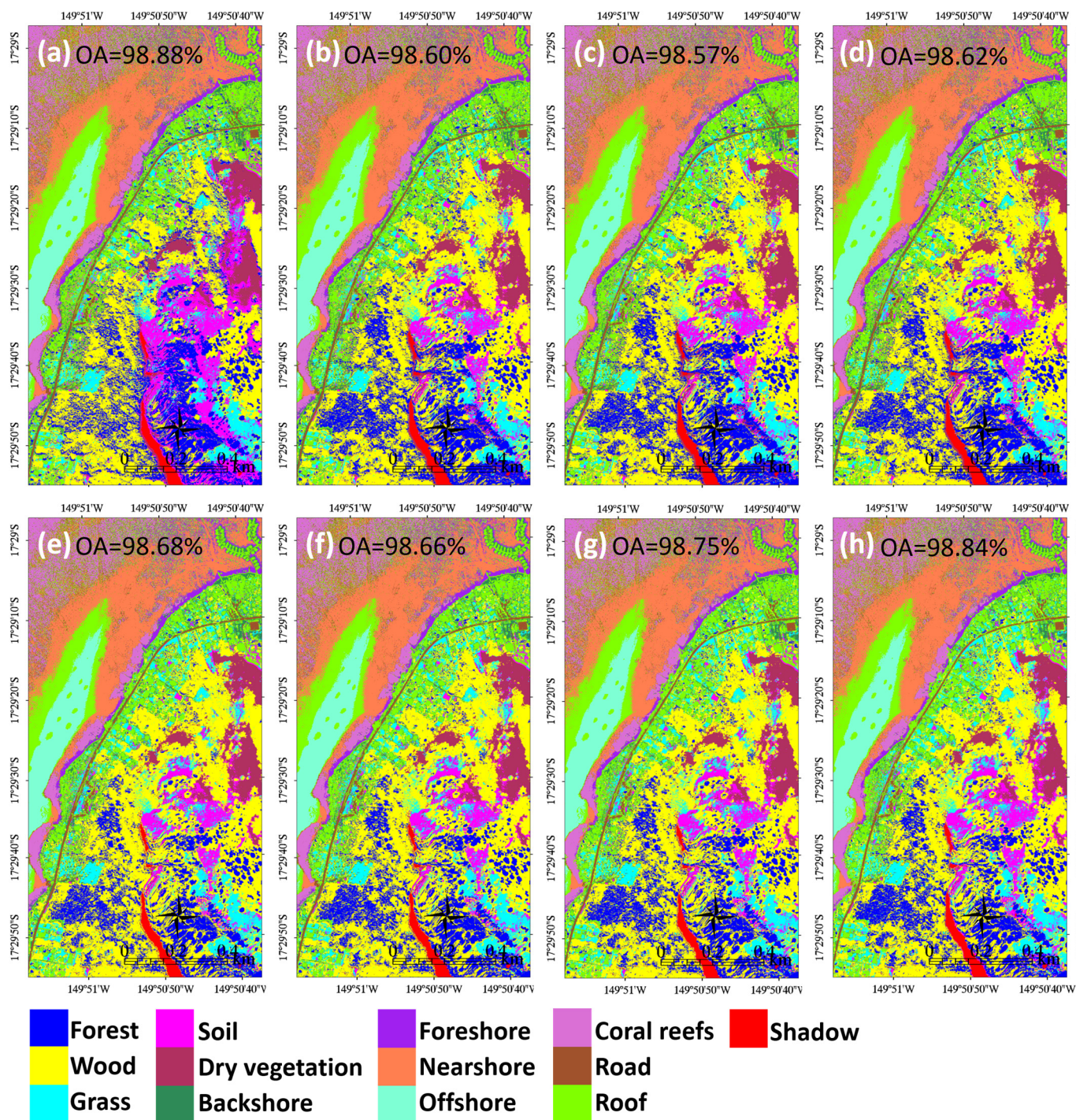
Figure 8. Maximum likelihood classification maps of the land-sea coral reefscape using WorldView-3 topobathymetric digital surface model and optical dataset with: (**a**) Mid-InfraRed1 (MIR1); (**b**) MIR2; (**c**) MIR3; (**d**) MIR4; (**e**) MIR5; (**f**) MIR6; (**g**) MIR7; (**h**) MIR8.

No topobathymetry DSM

Optical

	Forest	Wood	Grass	Soil	Dry vegetation	Backshore	Foreshore	Nearshore	Offshore	Coral reefs	Road	Roof	Shadow
Forest	0.23	-1.1	-1.9	-0.93	-1.07	0	0	0	0	0	-0.2	0	0
Wood	0.23	19.27	-25.87	-1.47	0	0	0	0	0	-0.07	0	0	0
Grass	-0.4	-18.17	27.7	1.43	0	0	0	0	0	0	0.03	0	0
Soil	-0.03	0	0	2.07	-1.8	0	0	0	0	-0.37	-12.8	0.17	0
Dry vegetation	0	0	0	-0.6	3.53	0	0	0	0	0	-0.23	-0.03	0
Backshore	0	0	0	0.07	0	-0.47	-0.67	0	0	0	0	-0.2	0
Foreshore	0	0	0	0	0	-0.3	0.43	-0.07	0	0	0	-1.03	0
Nearshore	0	0	0	0	0	0	-0.07	-0.1	0	-0.5	0	0	0
Offshore	0	0	0	0	0	0	0	0	0.07	-0.93	0	0	0
Coral reefs	0	0	0	-0.07	-0.37	0	0	-0.07	0	1.2	-0.03	0.03	-0.13
Road	0	0	0	-0.5	-0.43	0	-0.07	0.2	0	0.03	15.93	0.33	0
Roof	-0.03	0	0.07	0	0.13	0.77	0.37	0.03	-0.07	0.63	-2.7	0.73	0
Shadow	0	0	0	0	0	0	0	0	0	0	0	0	0.13

Topobathymetry DSM

	Forest	Wood	Grass	Soil	Dry vegetation	Backshore	Foreshore	Nearshore	Offshore	Coral reefs	Road	Roof	Shadow
Forest	5.43	-7.93	-1.9	-0.93	-1.07	0	0	0	0	0	-0.2	0	0
Wood	-5	26.27	-25.87	-1.37	0	-0.07	0	0	0	-0.07	0	0	0
Grass	-0.43	-18.33	27.5	0.67	0	0	0	0	0	0	0	0	0
Soil	0.03	0	0	8.53	-2.1	0	0	0	0	-0.43	-13.6	-5.23	0
Dry vegetation	0	0	0	-8.93	3.97	0	0	0	0	0	-0.23	-0.03	0
Backshore	0	0	0	3.13	0	1.2	-0.73	0	0	0.07	0.1	-2.53	0
Foreshore	0	0	0	0	0	-0.3	0.53	-0.13	0	0.03	0	-1.03	0
Nearshore	0	0	0	0	0	0	-0.07	0.27	0	-0.57	0	0	0
Offshore	0	0	0	0	0	0	0	0	0.07	-0.93	0	0	0
Coral reefs	0	0	0	-0.07	-0.37	0	0	-0.07	0	1.87	-0.03	0	-0.13
Road	0	0	0	-2.13	-0.43	0	-0.07	-0.07	0	-0.1	19.27	-15.03	0
Roof	-0.03	0	0.27	1.1	0	-0.83	0.33	0	-0.07	0.13	-5.3	23.87	0
Shadow	0	0	0	0	0	0	0	0	0	0	0	0	0.13

MIR8

Best Optical+MIR

	Forest	Wood	Grass	Soil	Dry vegetation	Backshore	Foreshore	Nearshore	Offshore	Coral reefs	Road	Roof	Shadow
Forest	5.43	-7.23	-1.9	-0.93	-1.07	0	0	0	0	0	-0.2	0	0
Wood	-4.93	25.53	-25.87	-1.5	0	-0.07	0	0	0	-0.07	0	0	0
Grass	-0.43	-18.3	27.6	-0.23	0	0	0	0	0	0	0	0	0
Soil	-0.03	0	0.13	14.6	-1.63	0	0	0	0	-0.43	-15.13	-1.9	0
Dry vegetation	0	0	0	-10.4	3.5	0	0	0	0	0	-0.23	-0.03	0
Backshore	0	0	0	0.47	0	1.97	-0.73	0	0	0	0.67	-5.03	0
Foreshore	0	0	0	0	0	-0.3	0.5	-0.13	0	0.03	0	-1.03	0
Nearshore	0	0	0	0	0	0	-0.07	0.27	0	-0.93	0	0	0
Offshore	0	0	0	0	0	0	0	0	0.07	-0.93	0	0	0
Coral reefs	0	0	0	-0.07	-0.37	0	0	-0.07	0	2.07	-0.03	0	-0.13
Road	0	0	0	-2.13	-0.43	0	-0.07	-0.1	0	-0.13	20.03	-14.87	0
Roof	-0.03	0	0.03	0.2	0	-1.6	0.37	0.03	-0.07	0.4	-5.1	22.87	0.03
Shadow	0	0	0	0	0	0	0	0	0	0	0	0	0.1

MIR1

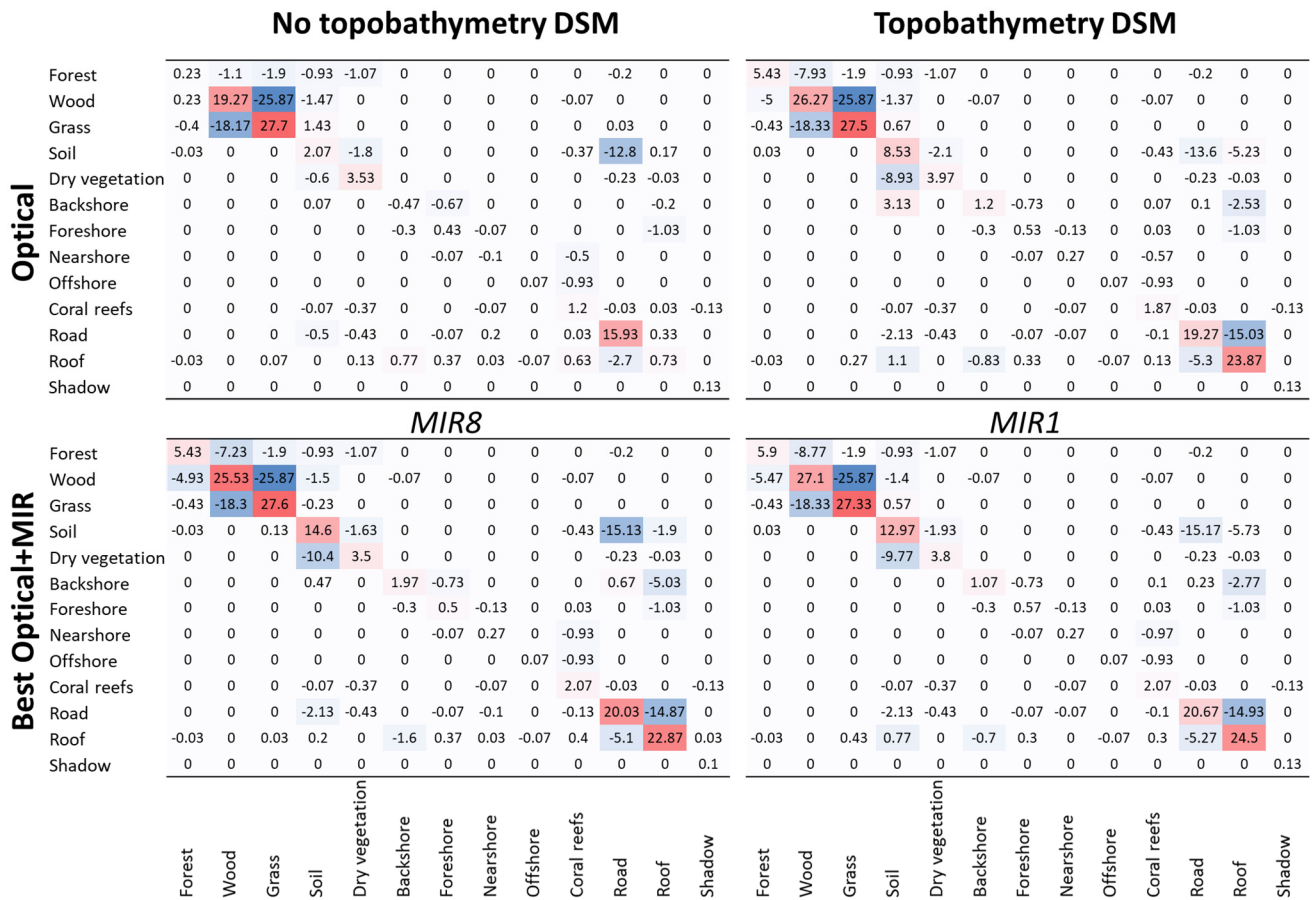|	Forest	Wood	Grass	Soil	Dry vegetation	Backshore	Foreshore	Nearshore	Offshore	Coral reefs	Road	Roof	Shadow
Forest	5.9	-8.77	-1.9	-0.93	-1.07	0	0	0	0	0	-0.2	0	0
Wood	-5.47	27.1	-25.87	-1.4	0	-0.07	0	0	0	-0.07	0	0	0
Grass	-0.43	-18.33	27.33	0.57	0	0	0	0	0	0	0	0	0
Soil	0.03	0	0	12.97	-1.93	0	0	0	0	-0.43	-15.17	-5.73	0
Dry vegetation	0	0	0	-9.77	3.8	0	0	0	0	0	-0.23	-0.03	0
Backshore	0	0	0	0	0	1.07	-0.73	0	0	0.1	0.23	-2.77	0
Foreshore	0	0	0	0	0	-0.3	0.57	-0.13	0	0.03	0	-1.03	0
Nearshore	0	0	0	0	0	0	-0.07	0.27	0	-0.97	0	0	0
Offshore	0	0	0	0	0	0	0	0	0.07	-0.93	0	0	0
Coral reefs	0	0	0	-0.07	-0.37	0	0	-0.07	0	2.07	-0.03	0	-0.13
Road	0	0	0	-2.13	-0.43	0	-0.07	-0.07	0	-0.1	20.67	-14.93	0
Roof	-0.03	0	0.43	0.77	0	-0.7	0.3	0	-0.07	0.3	-5.27	24.5	0
Shadow	0	0	0	0	0	0	0	0	0	0	0	0	0.13

Figure 9. Confusion matrices of the percent differences between the WorldView-3 basic blue-green-red classification validation and the best results for multispectral and superspectral combinations, deprived of and provided with WorldView-3 topobathymetric DSM.

4. Discussion

It is necessary to bear in mind that the mapping assessment was based on the surveyed calibration/validation rectangles (see Figure 1b). The use of a reliable and detailed ground-truth image is important for providing a comprehensive estimation of the area, thus preventing misclassifications detected by visual discrepancies as seen for the roof class rectangles that were mapped into the sea.

4.1. Land-Sea Coral Reefscape Mapping with a Multispectral WorldView-3 Stereo-Imagery

Together with its predecessor the 2009 WorldView-2, the 2014 WorldView-3 remains the state-of-the-science sub-metre spaceborne optical sensor, leveraging two extra spectral bands in the VIS and two supplementary spectral bands in the NIR gamut, compared to all other sub-metre competitors (see Introduction). The use of the five-band VIS and eight-band optical data showed a greater classification performance of the land-sea coral reefscape than did the basic BGR, namely a gain of 2.69% and 8.79%. These results are in strong agreement with the WorldView-2 multispectral Moorea land-sea mapping project [11].

Even if the satellite-based topography, on the one hand, and bathymetry, on the other hand, are commonly studied for sub-metre optical sensors [12,15], it is still innovative to create satellite-based merged topobathymetry: Pleiades-1 [25], WorldView-3 [24]. The RMSE validation accuracies of the photogrammetry-based topography and ratio-transformed bathymetry of 1.11 m ($R^2 = 0.99$, min = 20.26 m, max = 370.25 m, $N = 12$) and 0.89 m ($R^2 = 0.73$, min = −12.49 m, max = 0 m, $N = 15$), computed here, are also in concordance with the stereo-WorldView-3 multispectral Moorea land-sea mapping [24]. Even if the topographic accuracy was lower than the bathymetric one, an in-depth examination showed

that the accuracy rapidly diminished with depth, with a break at -5 m. In contrast, the accuracy of the altitude estimation remains constant even for higher values around 400 m. The bathymetry modeling could be ameliorated by using more soundings from a more recent survey, such as the topobathymetric LiDAR campaign locally operated in 2015. Further investigation will assess the influence of various pansharpening methods on those relief accuracies. Like the current work, this previous research highlighted that the addition of the topobathymetric DSM augmented the classification accuracy derived from the WorldView-3 basic BGR (2.74%), VIS (5.44%), and optical (9.15%) datasets. It is worth emphasizing that the DSM contribution:

- To the basic BGR neared the sole VIS performance ($\approx$2.7%);
- To the VIS prediction equaled 2.7%;
- To the optical accuracy approximated 6.4%.

4.2. Land-Sea Coral Reefscape Mapping with a Superspectral WorldView-3 Stereo-Imagery

The greatest novelty of the WorldView-3 resides in the collection of the eight-band MIR spectral bands, doubling the spectral bands of the WorldView-2 and extending the spectrum to 2365 nm [27]. The individual contributions of the eight MIR bands all contributed to the gain in classification accuracy of the land-sea coral reefscape compared to the basic mapping performance, ranging from 9.47% (MIR1) to 9.58% (MIR8), through 9.57% (MIR7). These significant inputs corresponded to a boosting of the optical (VIS+NIR) prediction, ranging from 0.68% to 0.79%.

The topobathymetric DSM reinforced the classification accuracy derived from the WorldView-3 optical datasets provided with the eight MIR bands. The best performances were here ensured by the MIR1 (9.73%), then the MIR8 (9.69%), while the least gain was attributed to the MIR3 (9.42%). Referenced to the optical dataset, the DSM therefore ameliorated the classification of:

- 0.94% with MIR1;
- 0.90% with MIR8;
- 0.63% with MIR3.

4.3. Land-Sea Coral Reefscape Mapping at the Class Scale

As might be logically expected, the best multispectral combination relied on the full optical dataset, from Coastal to NIR2. Relatively to the BGR discrete prediction, the discrimination between grass, wood and road classes were significantly refined. These findings might easily be explained if the NIR enhancement can capture the higher reflectance of both the chlorophyll-laden and the tar/asphalt -made classes better than the VIS one [30].

The DSM fusion with the optical dataset strongly improved the roof and the soil detection. This boosting was correlated with the decrease in misclassification with topographically lower road and topographically higher dry vegetation, respectively. The knowledge of the elevation component within the landscape therefore helped separate human-made, on the one hand, and natural features, on the other hand, that are spectrally similar in the optical range [30].

The best superspectral combination relied on the merge of the optical dataset with the MIR8 (2295–2365 nm). The positive effect at the class scale was tangible with grass, wood, roof, road and soil classes. Compared to the optical dataset, the roof and soil classes were better isolated. The roof outcome might stem from the MIR8 spectral fitting with the higher reflectance of the Polynesian roof made of oxidized-galvanized steel metal (0.34 reflectance) than the optical one (0.19 reflectance) [30]. The soil gain might also be due to MIR8 matching more closely with the higher reflectance (0.44) than the optical one (0.28) (see "brown loam" in [28]). These explanations were also supported by the decline in both roof and soil misclassifications with road, that displays a low MIR8 reflectance of 0.08 [30].

The DSM influence showed a better OA with the combination of the optical dataset with the MIR1 (1195–1225 nm). This optimum simply reinforced its positive effect on the

same previous classes, suggesting that the additional elevation information was relatively redundant to this coming from the MIR.

Concerning the coral reefs, the successive integration of the optical bands and the DSM to the BGR dataset, slightly but consistently, strengthened their detection. The addition of the Coastal and yellow bands favoured the coral reefs' separability among other benthic features given the refinement in spectral signatures [11]. The benthic terrain information was also profitable due to the robustness of the depth proxy for delineating benthos' ecophysiological belts [23]. In view of the neat classification of the coral reefs along the lagoon width (Figures 5–8), further research should divide the coral reefs' current class according to their landscape position (fringing, barrier and outer reefs), and their morphology (encrusting, branching, massive, tabular, columnar, etc.).

5. Conclusions

The superspectral WorldView-3 providing 16 bands, from 400 to 2365 nm, pansharpened at 0.3 m, was acquired in the form of stereo-imagery. Both topographic and bathymetric DSMs were built using a handful of ground and sea control points, enabling us to calibrate/validate the land-based photogrammetry and the sea-based radiative transfer model, provided with 1.11 and 0.89 m vertical accuracy, respectively. The best superspectral combination for enhancing the land-sea mapping of 13 habitats relied on the merging of the optical dataset (VIS+NIR) and the MIR8, which enhanced the basic BGR classification accuracy by 9.58%, thus reaching an OA of 98.73%. The classes that most benefited from this were the land use "roof" and land cover "soil" classes. The "coral reefs" consisted of the sea class that was the most favoured. The addition of the satellite-derived topobathymetric DSM to the optical+MIR1 was the best full combination, increasing the basic BGR classification accuracy by 9.73%, thus reaching an OA of 98.88%. The discrimination of the "roof" and "soil" classes was also strengthened, but the "coral reefs" remained constant.

Author Contributions: Conceptualization, A.C. and M.A.; methodology, A.C., D.L. and J.C.; software, A.C. and M.A.; validation, A.C.; formal analysis, A.C.; investigation, A.C. and J.C.; resources, A.C. and M.A.; data curation, A.C. and M.A.; writing—original draft preparation, A.C.; writing—review and editing, A.C., M.A., D.L. and J.C.; visualization, A.C. and M.A.; supervision, A.C. and J.C.; project administration, A.C. and J.C.; funding acquisition, M.A. All authors have read and agreed to the published version of the manuscript.

Conflicts of Interest: The authors declare no conflict of interest.

References

1. Costanza, R.; De Groot, R.; Sutton, P.; van der Ploeg, S.; Anderson, S.J.; Kubiszewski, I.; Farber, S.; Turner, R.K. Changes in the global value of ecosystem services. *Glob. Environ. Chang.* **2014**, *26*, 152–158. [CrossRef]
2. Spalding, M.; Burke, L.; Wood, S.A.; Ashpole, J.; Hutchison, J.; zu Ermgassen, P. Mapping the global value and distribution of coral reef tourism. *Mar. Policy* **2017**, *82*, 104–113. [CrossRef]
3. Spalding, M.; Spalding, M.D.; Ravilious, C.; Green, E.P. *World Atlas of Coral Reefs*; UNEP-WCMC: Cambridge, UK, 2001.
4. Hughes, T.P.; Barnes, M.L.; Bellwood, D.R.; Cinner, J.E.; Cumming, G.S.; Jackson, J.B.; Kleypas, J.; Van De Leemput, I.A.; Lough, J.M.; Morrison, T.H.; et al. Coral reefs in the Anthropocene. *Nature* **2017**, *546*, 82–90. [CrossRef] [PubMed]
5. Collin, A.; Hench, J.L. Towards Deeper Measurements of Tropical Reefscape Structure Using the WorldView-2 Spaceborne Sensor. *Remote Sens.* **2012**, *4*, 1425–1447. [CrossRef]
6. Mancini, F.; Dubbini, M.; Gattelli, M.; Stecchi, F.; Fabbri, S.; Gabbianelli, G. Using Unmanned Aerial Vehicles (UAV) for High-Resolution Reconstruction of Topography: The Structure from Motion Approach on Coastal Environments. *Remote Sens.* **2013**, *5*, 6880–6898. [CrossRef]
7. Agrafiotis, P.; Karantzalos, K.; Georgopoulos, A.; Skarlatos, D. Correcting Image Refraction: Towards Accurate Aerial Image-Based Bathymetry Mapping in Shallow Waters. *Remote Sens.* **2020**, *12*, 322. [CrossRef]
8. Collin, A.M.; Andel, M.; James, D.; Claudet, J. The Superspectral/Hyperspatial Worldview-3 as The Link between Spaceborne Hyperspectral and Airborne Hyperspatial Sensors: The Case Study of the Complex Tropical Coast. *Int. Arch. Photogramm. Remote Sens. Spat. Inf. Sci.* **2019**, *XLII-2/W13*, 1849–1854. [CrossRef]

9. Collin, A.; Long, B.; Archambault, P. Merging land-marine realms: Spatial patterns of seamless coastal habitats using a multispectral LiDAR. *Remote Sens. Environ.* **2012**, *123*, 390–399. [CrossRef]
10. Mury, A.; Collin, A.; James, D. Morpho–Sedimentary Monitoring in a Coastal Area, from 1D to 2.5D, Using Airborne Drone Imagery. *Drones* **2019**, *3*, 62. [CrossRef]
11. Collin, A.; Archambault, P.; Planes, S. Bridging Ridge-to-Reef Patches: Seamless Classification of the Coast Using Very High Resolution Satellite. *Remote Sens.* **2013**, *5*, 3583–3610. [CrossRef]
12. James, D.; Collin, A.; Mury, A.; Costa, S. Very high resolution land use and land cover mapping using pleiades-1 stereo imagery and machine learning. *Int. Arch. Photogramm. Remote Sens. Spat. Inf. Sci.* **2020**, *XLIII-B2-2*, 675–682. [CrossRef]
13. Collin, A.; Planes, S. Enhancing Coral Health Detection Using Spectral Diversity Indices from WorldView-2 Imagery and Machine Learners. *Remote Sens.* **2012**, *4*, 3244–3264. [CrossRef]
14. Collin, A.; Hench, J.L.; Planes, S. A novel spaceborne proxy for mapping coral cover. In Proceedings of the 12th International Coral Reef Symposium, Cairns, Australia, 9–13 July 2012.
15. Collin, A.; Etienne, S.; Feunteun, E. VHR coastal bathymetry using WorldView-3: Colour versus learner. *Remote Sens. Lett.* **2017**, *8*, 1072–1081. [CrossRef]
16. Kruse, F.A.; Baugh, W.M.; Perry, S.L. Validation of DigitalGlobe WorldView-3 Earth imaging satellite shortwave infrared bands for mineral mapping. *J. Appl. Remote Sens.* **2015**, *9*, 96044. [CrossRef]
17. Asadzadeh, S.; Filho, C.R.D.S. Investigating the capability of WorldView-3 superspectral data for direct hydrocarbon detection. *Remote Sens. Environ.* **2016**, *173*, 162–173. [CrossRef]
18. Ye, B.; Tian, S.; Ge, J.; Sun, Y. Assessment of WorldView-3 Data for Lithological Mapping. *Remote Sens.* **2017**, *9*, 1132. [CrossRef]
19. Collin, A.; Lambert, N.; Etienne, S. Satellite-based salt marsh elevation, vegetation height, and species composition mapping using the superspectral WorldView-3 imagery. *Int. J. Remote Sens.* **2018**, *39*, 5619–5637. [CrossRef]
20. Ferreira, M.P.; Wagner, F.H.; Aragão, L.E.; Shimabukuro, Y.E.; Filho, C.R.D.S. Tree species classification in tropical forests using visible to shortwave infrared WorldView-3 images and texture analysis. *ISPRS J. Photogramm. Remote Sens.* **2019**, *149*, 119–131. [CrossRef]
21. Guo, X.; Li, P. Mapping plastic materials in an urban area: Development of the normalized difference plastic index using WorldView-3 superspectral data. *ISPRS J. Photogramm. Remote Sens.* **2020**, *169*, 214–226. [CrossRef]
22. Collin, A.; Hench, J.L.; Pastol, Y.; Planes, S.; Thiault, L.; Schmitt, R.J.; Holbrook, S.J.; Davies, N.; Troyer, M. High resolution topobathymetry using a Pleiades-1 triplet: Moorea Island in 3D. *Remote Sens. Environ.* **2018**, *208*, 109–119. [CrossRef]
23. Collin, A.; Nadaoka, K.; Nakamura, T. Mapping VHR Water Depth, Seabed and Land Cover Using Google Earth Data. *ISPRS Int. J. Geo Inform.* **2014**, *3*, 1157–1179. [CrossRef]
24. Collin, A.; Andel, M.; Lecchini, D.; Claudet, J. Submeter 3D ridge-to-reef classification using a WorldView-3 satellite stereoimagery. In Proceedings of the 14th International Coral Reef Symposium, Bremen, Germany, 5–10 July 2020.
25. Davies, N.; IDEA Consortium; Field, D.; Gavaghan, D.; Holbrook, S.J.; Planes, S.; Troyer, M.; Bonsall, M.; Claudet, J.; Roderick, G.; et al. Simulating social-ecological systems: The Island Digital Ecosystem Avatars (IDEA) consortium. *GigaScience* **2016**, *5*, 14. [CrossRef]
26. Institut de la Statistique de Polynesie Française. *Le Recensement de la Population en Polynésie Française en 2017*; ISPF: Papeete, French Polynesia, 2018.
27. Kwan, C.; Budavari, B.; Bovik, A.C.; Marchisio, G. Blind Quality Assessment of Fused WorldView-3 Images by Using the Combinations of Pansharpening and Hypersharpening Paradigms. *IEEE Geosci. Remote Sens. Lett.* **2017**, *14*, 1835–1839. [CrossRef]
28. Xu, F.; Woodhouse, N.; Xu, Z.; Marr, D.; Yang, X.; Wang, Y. Blunder elimination techniques in adaptive automatic terrain extraction. *ISPRS J.* **2008**, *29*, 21.
29. Stumpf, R.P.; Holderied, K.; Sinclair, M. Determination of water depth with high-resolution satellite imagery over variable bottom types. *Limnol. Oceanogr.* **2003**, *48*, 547–556. [CrossRef]
30. Baldridge, A.; Hook, S.; Grove, C.; Rivera, G. The ASTER spectral library version 2.0. *Remote Sens. Environ.* **2009**, *113*, 711–715. [CrossRef]